

# Variability, polarimetry, and timing properties of single pulses from PSR J2222–0137 using FAST

X. L. Miao<sup>1</sup> , <sup>\*</sup> W. W. Zhu<sup>1,2</sup> , <sup>†</sup> M. Kramer<sup>3,4</sup> , P. C. C. Freire<sup>3</sup> , L. Shao,<sup>5,1,3</sup> , M. Yuan<sup>1,7</sup> , L. Q. Meng<sup>1,7</sup> , Z. W. Wu<sup>1</sup> , C. C. Miao<sup>1,7</sup> , Y. J. Guo<sup>3</sup>, D. J. Champion<sup>3</sup> , E. Fonseca<sup>8,9,10,11</sup> , J. M. Yao<sup>12</sup>, M. Y. Xue<sup>1</sup> , J. R. Niu<sup>1,7</sup> , H. Hu<sup>3</sup> , C. M. Zhang<sup>1</sup>

<sup>1</sup>National Astronomical Observatories, Chinese Academy of Sciences, 20A Datun Road, Chaoyang District, Beijing 100101, China

<sup>2</sup>Institute for Frontiers in Astronomy and Astrophysics, Beijing Normal University, Beijing 102206, China

<sup>3</sup>Max-Planck Institut für Radioastronomie, Auf dem Hügel 69, D-53121 Bonn, Germany

<sup>4</sup>Jodrell Bank Centre for Astrophysics, Department of Physics and Astronomy, University of Manchester, M13 9PL Manchester, UK

<sup>5</sup>Kavli Institute for Astronomy and Astrophysics, Peking University, Beijing 100871, China

<sup>6</sup>Department of Astronomy, School of Physics, Peking University, Beijing 100871, China

<sup>7</sup>School of Astronomy and Space Science, University of Chinese Academy of Sciences, Beijing, 100049, China

<sup>8</sup>Department of Physics and Astronomy, West Virginia University, PO Box 6315, Morgantown, WV 26506, USA

<sup>9</sup>Center for Gravitational Waves and Cosmology, West Virginia University, Chestnut Ridge Research Building, Morgantown, WV 26505, USA

<sup>10</sup>Department of Physics, McGill University, 3600 rue University, Montréal, QC H3A 2T8, Canada

<sup>11</sup>McGill Space Institute, McGill University, 3550 rue University, Montréal, QC H3A 2A7, Canada

<sup>12</sup>Xinjiang Astronomical Observatory, Chinese Academy of Sciences, Urumqi, Xinjiang 830011, People's Republic of China

Accepted XXX. Received YYY; in original form ZZZ

## ABSTRACT

In our work, we analyse  $5 \times 10^4$  single pulses from the recycled pulsar PSR J2222–0137 in one of its scintillation maxima observed by the Five-hundred-meter Aperture Spherical radio Telescope (FAST). PSR J2222–0137 is one of the nearest and best studies of binary pulsars and a unique laboratory for testing gravitational theories. We report single pulses' energy distribution and polarization from the pulsar's main-pulse region. The single pulse energy follows the log-normal distribution. We resolve a steep polarization swing, but at the current time resolution ( $64 \mu\text{s}$ ), we find no evidence for the orthogonal jump in the main-pulse region, as has been suspected. We find a potential sub-pulse drifting period of  $P_3 \sim 3.5 P$ . We analyse the jitter noise from different integrated numbers of pulses and find that its  $\sigma_j$  is  $270 \pm 9$  ns for 1-hr integration at 1.25 GHz. This result is useful for optimizing future timing campaigns with FAST or other radio telescopes.

**Key words:** methods: data analysis - pulsars: individual: PSR J2222–0137

## 1 INTRODUCTION

Millisecond pulsars (MSPs, defined here in the broad sense of having been recycled by accretion of matter from their companions, see Tauris & van den Heuvel 2023) are neutron stars (NSs) known for their superb rotational stability. Like most pulsars, their integrated profiles are also stable; this means that we can obtain precise pulses' times of arrival (TOAs; there are also some exceptions, such as PSRs J1643–1224, J1713+0747, and see e.g. Shannon et al. 2016; Xu et al. 2021; Singha et al. 2021). This, combined with the fact that most MSPs are in binary systems, implies that we can use TOA analysis (pulsar timing) to measure their orbital motions with exquisite precision.

In some binary pulsars, consistent pulsar timing can detect - and precisely measure - relativistic perturbations to the orbital motion and the propagation of radio waves in the system. If enough relativis-

tic effects are detected in the same system, we can obtain rigorous tests of gravity theories (Taylor & Weisberg 1982, 1989; Damour & Taylor 1992; Freire et al. 2012; Voisin et al. 2020; Kramer et al. 2021; Shao 2023, for reviews see Wex 2014; Hu et al. 2023). For a broader class of binaries, the measurement of these relativistic effects allows measurements of NS masses, which is important for several reasons, mostly the study of the unknown properties of the super-dense matter at the centre of a NS (Özel & Freire 2016). Irrespective of the detection of relativistic effects in their orbits, bright MSPs are also crucial for nHz-gravitational wave (GW) detection by pulsar timing arrays (PTAs, Estabrook & Wahlquist 1975; Detweiler 1979; Hellings & Downs 1983; van Haasteren et al. 2009); in these experiments, the TOA accuracy determines the sensitivity of PTAs to nHz-GWs detection. Recently, four independent PTA groups have found the critical evidence of nHz-GW background (Xu et al. 2023; Reardon et al. 2023; Antoniadis et al. 2023; Agazie et al. 2023), and we are in the era of opening the nHz-GW observation window.

<sup>\*</sup> E-mail: xlmiao@nao.cas.cn

<sup>†</sup> E-mail: zhuww@nao.cas.cn

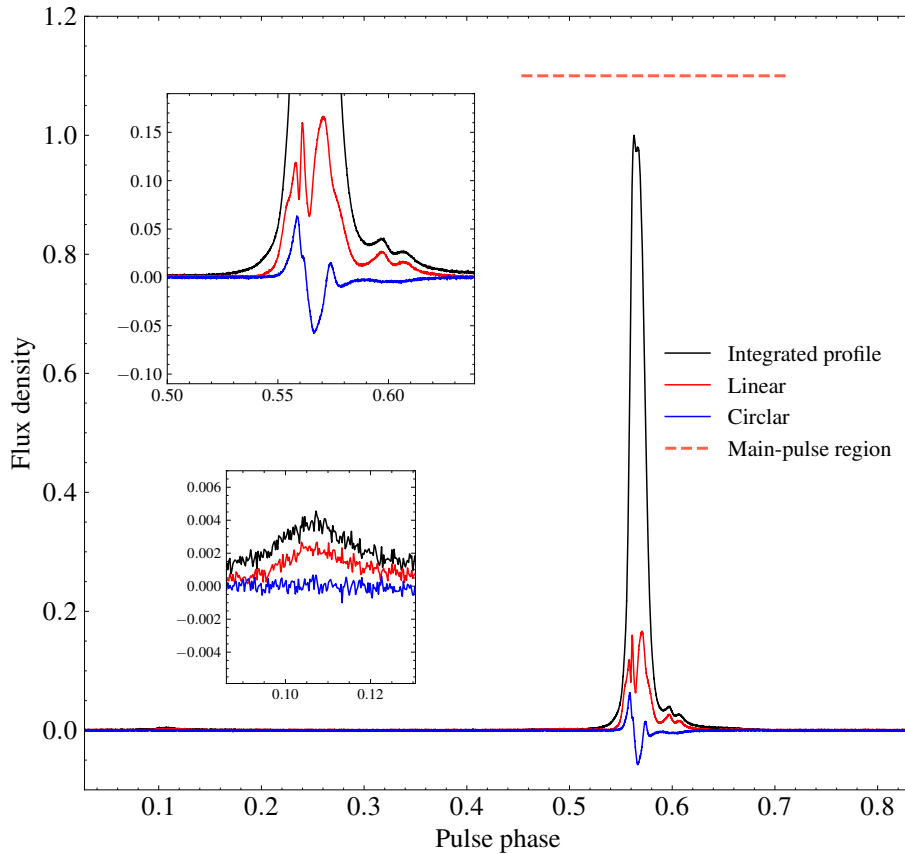


**Figure 1.** The polarization profile of PSR J2222–0137 is observed by FAST at a central frequency of 1250 MHz on MJD 59209, and it is averaged over a bandwidth of 420 MHz. The black line is the total intensity (SNR $\sim$ 23000) of the integration time of 30 min, the red line is the linear polarization intensity, and the blue line is the circular polarization intensity. The upper inset shows an enlarged version of the main pulse, and the bottom inset shows an enlarged version of the interpulse which was first detected by FAST. The red dashed line marks the selected main-pulse region used for single-pulse analysis.

### 1.1 PSR J2222–0137: a nearby laboratory for gravity theories

Among the best laboratories for tests of gravity theories is PSR J2222–0137, a recycled pulsar with a massive white dwarf (WD) companion in a 2.44-day orbit (Kaplan et al. 2014). The system has an edge-on orbit, allowing a highly precise measurement of the Shapiro delay (Shapiro 1964), which provides an accurate mass measurement for the pulsar and its WD companion,  $1.831 \pm 0.010 M_{\odot}$  and  $1.319 \pm 0.004 M_{\odot}$  respectively. The large masses for the pulsar and WD companion make it the most massive double degenerate binary pulsar known in our Galaxy, with a total mass of  $3.150 \pm 0.014 M_{\odot}$ . In this system, we can also obtain a significant measurement of the rate of advance of periastron  $\dot{\omega}$ , which provides a redundant measurement of the system’s total mass and a 1% test of GR, which the theory passes (Guo et al. 2021).

Furthermore, being one of the nearest binary pulsars, it has a precise distance measurement,  $d = 268.1^{+1.2}_{-1.1}$  pc, by Very Long Baseline Interferometry (Deller & et al. 2013; Guo et al. 2021). This and the precise timing results in a precisely measured intrinsic orbital period variation,  $\dot{P}_b^{\text{intr}} = -0.0143 \pm 0.0076 \times 10^{-12} \text{ s s}^{-1}$  (Guo et al. 2021).

These measurements are important because the close agreement between  $\dot{P}_b^{\text{intr}}$  and the GR prediction provides a tight limit on the emission of dipolar gravitational waves (DGW) from this system (Guo et al. 2021; Batrakov et al. 2023), a phenomenon generally predicted by alternative theories of gravity (Eardley 1975). Furthermore, the pulsar mass places it in a NS mass range that had previously not been probed by precise tests of GW emission, where the phenomenon

of spontaneous scalarisation (a large increase of DGW emission predicted by some alternative gravity theories, like those of Damour & Esposito-Farese 1993) is still possible. For this reason, the DGW emission limit for PSR J2222–0137 represents a powerful constraint on that phenomenon (Zhao et al. 2022; Batrakov et al. 2023).

### 1.2 FAST observations of PSR J2222–0137

The high sensitivity of the Five-hundred-meter Aperture Spherical radio Telescope (FAST) allows us to measure the emission of PSR J2222–0137 with high precision. The main aim of these observations is to improve the precision of the tests of gravity theories with this pulsar. However, even before that, the FAST data from this pulsar - particularly during a scintillation maximum - have already provided an extremely high signal-to-noise ratio (SNR) integrated profile. This resulted in an improved polarization study and revealed the existence of an interpulse for the first time. These measurements were crucial for determining the large-scale structure of the magnetic field of the pulsar, which allowed an estimate of the spin and orbital geometry of this pulsar - which was confirmed independently by timing measurements (Guo et al. 2021).

The scintillation maxima data from PSR J2222–0137 is also useful for a single-pulse analysis. In general, the integration of hundreds or thousands of pulse periods leads to stable profiles; this is the fundamental assumption of pulsar timing, which allows us to measure pulsar parameters with high precision. However, the single-

pulse shape changes stochastically from pulse to pulse, and some of them exhibit special temporal characteristics, like sub-pulses drifting (Drake & Craft 1968; Weltevrede et al. 2006), mode change (Bartel et al. 1982), nulling (Backer 1970; Edwards & Stappers 2003; Wang et al. 2007), giant pulses (Staelin & Reifenstein 1968; Hankins et al. 2003), and microstructure in single pulses (Cordes et al. 1990; Mitra et al. 2015; De et al. 2016; Liu et al. 2022). These temporal characteristics in single pulses are often found in normal pulsars but are uncommon in MSPs.

This pulse-to-pulse variability results in the pulse phase jitter phenomenon in integrated profiles (Cordes & Downs 1985; Cordes 1993; Cordes & Shannon 2010), a trivial consequence of the fact that it takes significant time and pulse averaging for the integrated pulse to get close to “the” average pulse profile of the pulsar. These small variations of the integrated pulse profile limit the timing precision of MSPs and influence the ability of test gravity and PTAs to detect nHz GW.

A comprehensive study of single pulse variability in MSPs could help understand the limits of the timing precision (Osłowski et al. 2011; Imgrund et al. 2015). For a long time, the limited telescope sensitivity of most radio telescopes implied that only the single pulses of a handful of the brightest MSPs could be studied (Shannon & Cordes 2012; Liu et al. 2014). The high sensitivity of FAST allows us to investigate more MSPs, and these investigations can lead to advances not only in understanding the limitations of their timing precision, but also in our understanding of the emission physics of pulsars. For PSR J2222–0137, the jitter phenomenon is evident in high SNR observations from FAST. Therefore, it is important to study the jitter noise of PSR J2222–0137 to optimise future timing campaigns with FAST or other high-sensitivity radio telescopes.

As mentioned above, the polarization profiles of pulsars can provide important information about their geometry. A commonly used model is the rotating vector model (RVM, Radhakrishnan et al. 1969), which describes the variations in the linear polarization position angle (PPA) of many pulsars well. However, some pulsars’ linear PPA show rapid jumps of  $90^\circ$ , which deviate from a standard RVM. Such jumps are believed to come from the presence of two orthogonal polarization modes in the radiation and are called orthogonal polarization modes (OPMs) (Gil & Lyne 1995; Edwards & Stappers 2004). Guo et al. (2021)’s figure 1 shows the integrated polarization profile of PSR J2222–0137, and the authors suggest that the marked grey region of the PPA of the linear emission results from OPMs. In this work, we will analyse this particular polarization jump by resolving it through single pulse polarization measurements and investigate the above interpretation.

In this paper, we present a comprehensive analysis using the high SNR data of PSR J2222–0137. In Section 2, we describe the details of the observations and single pulse data analysis. In Section 3, we show the results of this analysis, including the single pulse energy distribution, pulse variability and polarization, and finally, an analysis of the integrated pulse jitter for PSR J2222–0137. We conclude and discuss our results in Section 4.

## 2 OBSERVATION AND DATA PROCESSING

In our FAST observation project, we have performed thirty 30-min observations of PSR J2222–0137. We used the central beam of the 19-beam receiver and the frequency range between 1000 and 1500 MHz with 4096 frequency channels. We used only the band between 1040 to 1460 MHz because of the decrease in sensitivity at the edges of the band (Jiang et al. 2020). We recorded the data in pulsar search

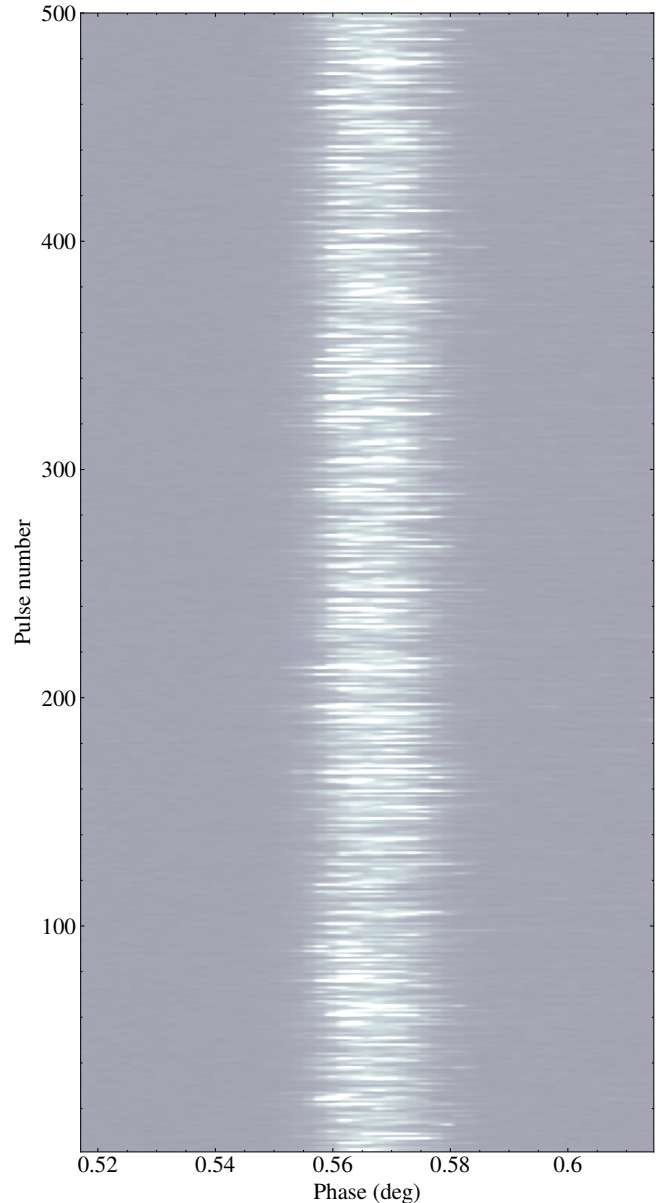


**Figure 2.** The pulse stack of PSR J2222–0137, we show the pulse-to-pulse variation of 500 continuous pulses, for a total duration of 16.4 s. The time resolution is  $64.06 \mu\text{s}$ , corresponding to the spin period divided by the 512 bins.

mode with full-Stokes information, and each observation starts with a 1-min calibration noise diode for the polarization calibration.

The pulsar often exhibits a  $\text{SNR} \sim 4000$  in a regular FAST observation. In this paper, we choose the brightest observation of PSR J2222–0137 from MJD 59209, when the pulsar was in a scintillation maximum with a  $\text{SNR} \sim 23000$ . Guo et al. (2021) already used this observation to improve the geometric parameters for the pulsar spin. Fig. 1 shows the integrated polarization profile of PSR J2222–0137 obtained from this observation. The interpulse is visible between spin phases 0.09 – 0.13 and is more clearly visible in the lower inset.

To get single pulses of PSR J2222–0137, we used the DSPSR<sup>1</sup> software package (van Straten & Bailes 2011) to extract individual pulses and remove inter-channel dispersion delays with the “-K” option. The data were coherently dedispersed using a dispersion measure (DM) of  $3.28 \text{ cm}^{-3} \text{ pc}$  (Guo et al. 2021). The spin period of PSR J2222–0137 is 32.81 ms and the time resolution we used is  $49.152 \mu\text{s}$ , so we set the number of phase bins to 512 for every pulse. We used the PSRCHIVE<sup>2</sup> software package (Hotan et al. 2004) to excise radio frequency interference (RFI) in every single pulse in the frequency domain. We used “psrzap” for every single pulse to excise RFI in the frequency domain. We recorded excised frequency channels for all single pulses. We combined the number of excised frequency channels and used the combined frequency channels to excise every single pulse again, ensuring that every pulse’s excised frequency channels are the same. We used the 1-min calibration noise files to calibrate polarization. We used “rmfit” to fit the Faraday rotation measure (RM) and got  $\text{RM} = 4.28 \pm 0.18 \text{ rad m}^{-2}$ . We derotated the stokes parameters according to this RM for every single pulse.

In our work, we concentrate on investigating the main-pulse properties, i.e., the spin phases between  $0.45 - 0.71$  marked by the red dashed line in Fig. 1, and  $0.72 - 0.98$  as the off-pulse region to provide the information on the noise. We obtained 52692 high-SNR single pulses from the main-pulse component. Fig. 2 shows an example of a pulse stack containing 500 consecutive pulses of the main pulse. It clearly shows the variation of intensity, shape, and phase from pulse to pulse.

We used the PSRSALSA<sup>3</sup> software (Weltevrede 2016) to analyse these single pulses. We used it to obtain the distribution of the main pulse and noise energy. We also used PSRSALSA to analyse the sub-pulse drifting. We used TEMPO<sup>4</sup> software to get pulse TOAs and timing residuals, and we used these timing residuals to do jitter analysis.

### 3 RESULTS

This section presents the results of the single pulse analysis of PSR J2222–0137. In Sec. 3.1, we provide the energy distributions of these single pulses, which we check for mode change, nulling, sub-pulse drifting, and giant pulse emission. In Sec. 3.2, we analyse the single pulse polarization. In Sec. 3.3, we provide a jitter noise investigation of PSR J2222–0137.

#### 3.1 Single pulse properties

During the MJD 59209 observation, the minimal single pulse SNR is  $\sim 8.7$ , and the maximal is  $\sim 531.6$ . These values of SNR are calculated by,

$$\text{SNR} = \frac{\sum I_i}{\sigma_{\text{off}} \sqrt{n}}, \quad (1)$$

where  $\sum I_i$  ( $I_i > 3\sigma_{\text{off}}$ ) is the sum of the intensity of the on-pulse region of single pulses,  $n$  is the number of sum bins, and  $\sigma_{\text{off}}$  is the Root-Mean-Square (RMS) intensity of the off-pulse region. All single pulses show a  $\text{SNR} > 8\sigma$ , in other words, we do not detect nulling.

<sup>1</sup> <http://dspsr.sourceforge.net>

<sup>2</sup> <http://psrchive.sourceforge.net>

<sup>3</sup> <https://github.com/weltevrede/psrsalsa>

<sup>4</sup> <https://tempo.sourceforge.net>

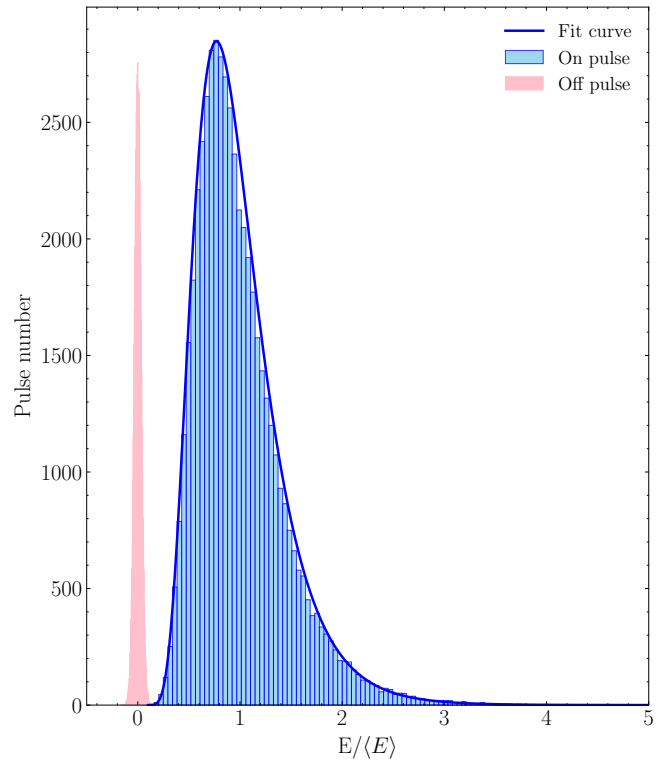


**Figure 3.** The energy distributions in the main pulse and the off-pulse regions. The sky-blue histogram is the main-pulse energy distribution, and the pink histogram is the noise energy distribution. The blue solid line is the fitted curve of the main-pulse energy distribution. The average pulse energy represents, in the observation being analysed, a SNR of 87.

The energy distribution of the main-pulse region is shown in Fig. 3. The energy distribution shows an obvious log-normal distribution. The log-normal probability density function is defined as,

$$P(E) = \frac{\langle E \rangle}{\sqrt{2\pi}\sigma E} \exp \left[ - \left( \ln \frac{E}{\langle E \rangle} - \mu \right)^2 / (2\sigma^2) \right], \quad (2)$$

where  $\langle E \rangle$  is the average energy of the main pulse of PSR J2222–0137; this corresponds to a SNR of 87. Using the main-pulse energy distribution, we fit Eq. (2) to the data to obtain the values of  $\mu = -0.1032 \pm 0.0021$  and  $\sigma = 0.4108 \pm 0.0018$ . Performing a KS-test, we get a p-value,  $p = 0.81$ , indicating that the log-normal distribution provides a very good description of the data. The fitted curve is the blue solid line in Fig. 3, where we see how closely the energy distribution of the main-pulse region conforms to a log-normal distribution. The off-pulse region follows a Gaussian distribution, corresponding to the noise’s energy distribution.

The highest single pulse energy of the single pulse on MJD 59209 is about  $6.9 \langle E \rangle$ . The definition of a giant pulse is a single pulse with energy above  $10 \langle E \rangle$  (Cairns 2004), so based on our results, there is no giant pulse in the PSR J2222–0137 data taken on MJD 59209. This is not unexpected since the pulse-energy distribution of giant pulses follows a power law. The log-normal energy distribution of single pulses of PSR J2222–0137 implies that the pulsar’s radiation follows a stochastic growth theory prediction (Robinson 1992; Cairns et al. 2001).

We compare the average pulse profiles selected from different ranges of SNR in Fig. 4, and the definition of SNR in Fig. 4 is Eq. (1). The black solid line is the total intensity profile. We can notice that the

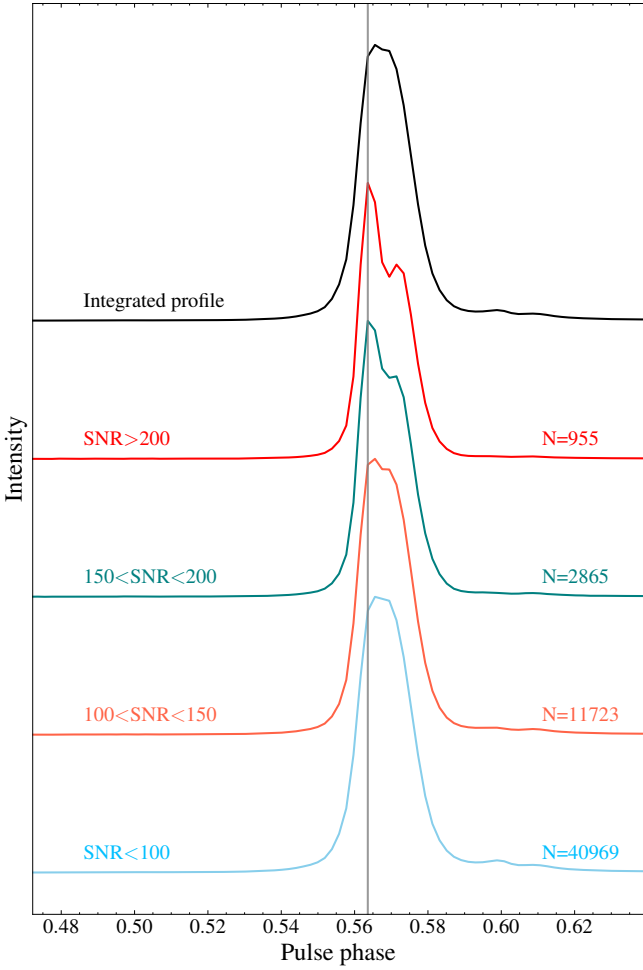


**Figure 4.** The average pulse profiles for different SNR ranges. The profiles are integrated by single pulses with different SNR ranges. The black solid line is the total intensity profile, the red solid line is the average pulse profile from single pulses with  $\text{SNR} > 200$ , the teal solid line is the average pulse profile from single pulses with  $150 < \text{SNR} < 200$ , the tomato solid line is the average pulse profile from single pulses with  $100 < \text{SNR} < 150$ , the sky-blue solid line is the average pulse profile from single pulses with  $\text{SNR} < 100$ . The grey solid vertical line marks the leading peak of the average pulse profile from single pulses with  $\text{SNR} > 200$ . The number of pulses averaged  $N$  of each SNR range is marked in the figure. The profiles are normalized by the peak value of every average pulse profile individually.

average pulse profile built using the brightest pulses is narrower than the total average profile, and the phase of the leading peak is earlier than the phase of the leading component of the main peak of the pulse profile (the grey solid vertical line). As the SNR of the single pulses decreases, the pulse profile resembles the total shape more and more, as we should expect, given that the weaker pulses are more numerous and contribute more energy to the pulse profile. This phenomenon indicates that the high SNR single pulses may have an earlier arrival time than the low SNR single pulses for PSR J2222–0137.

We provide the number density distribution of pulses with respect to their relative peak flux densities and spin phases where the pulse peaks occur in Fig. 5. Here, the pulses with higher peak flux densities concentrate in a narrow region corresponding to the leading peak of the total average profile. The pulses with lower peak flux densities are distributed in a wider region.

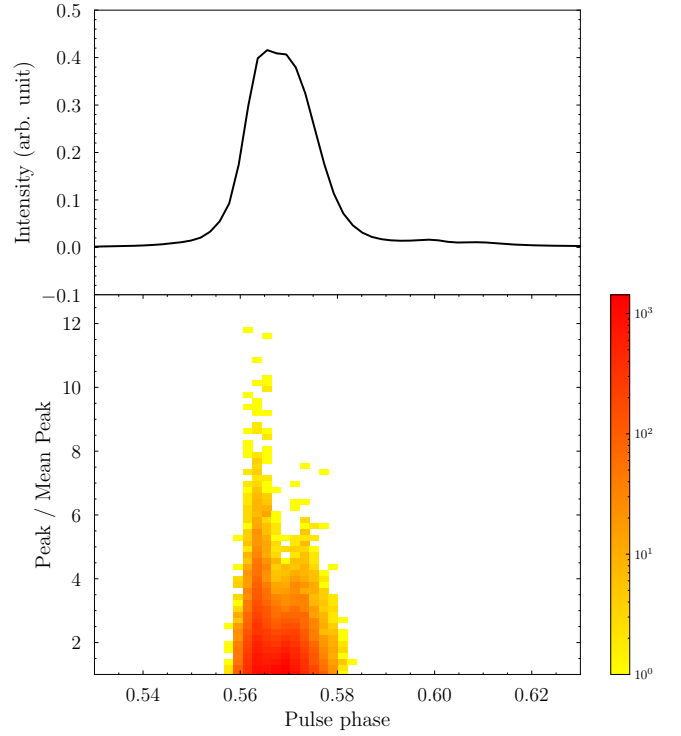


**Figure 5.** The upper panel is the total intensity profile. The lower panel is the number density distribution of pulses with respect to their peak flux density and the spin phase where that peak occurs. The time of each bin corresponds to  $64.06 \mu\text{s}$ .

We also plot the number density distribution of pulses in terms of their relative peak flux densities and the equivalent width  $W_{\text{eq}}$  in Fig. 6, and we define  $W_{\text{eq}}$  as the area under the pulse divided by the peak amplitude,

$$W_{\text{eq}} = \frac{\sum I_i}{I_p} \times \Delta t, \quad (3)$$

where  $I_p$  is the peak amplitude of single pulse and  $\Delta t = 64.06 \mu\text{s}$  is the time resolution. As can be seen, the  $W_{\text{eq}}$  of the main pulse of PSR J2222–0137 concentrates in about 0.5 ms. The bright pulses have smaller  $W_{\text{eq}}$ ,  $W_{\text{eq}} < 0.4$  ms, which is consistent with the result shown in Fig. 4 that high SNR pulses have a narrower profile. The weak pulses have a wider  $W_{\text{eq}}$  distribution.

In general, the position of each individual single pulse is random. If pulsars have sub-pulse drifting, the pulse-to-pulse variation is known to be regular. In order to study the properties of variation of the main pulse, we have calculated the longitude-resolved modulation index that measures the normalized RMS intensity across pulse phase  $i$  and it is defined as (Shannon & Cordes 2012),

$$m_{i, \text{on}} = \frac{\sqrt{\sigma_{i, \text{on}}^2 - \sigma_{\text{off}}^2}}{I_{i, \text{on}}}, \quad (4)$$

where  $I_{i, \text{on}}$  and  $\sigma_{i, \text{on}}$  are the mean and RMS intensity at pulse phase  $i$  of on-pulse region. We plot the modulation index  $m_i$  as a function of the pulse phase of PSR J2222–0137 in the top figure of Fig. 7. Except for the edge region of the integrated profile of the main-pulse region, the modulation indices are lower than 1. The values of  $m_i$  at the edges of the integrated profile indicate a significant change in the strength of pulses, commonly seen in normal pulsars. The large value

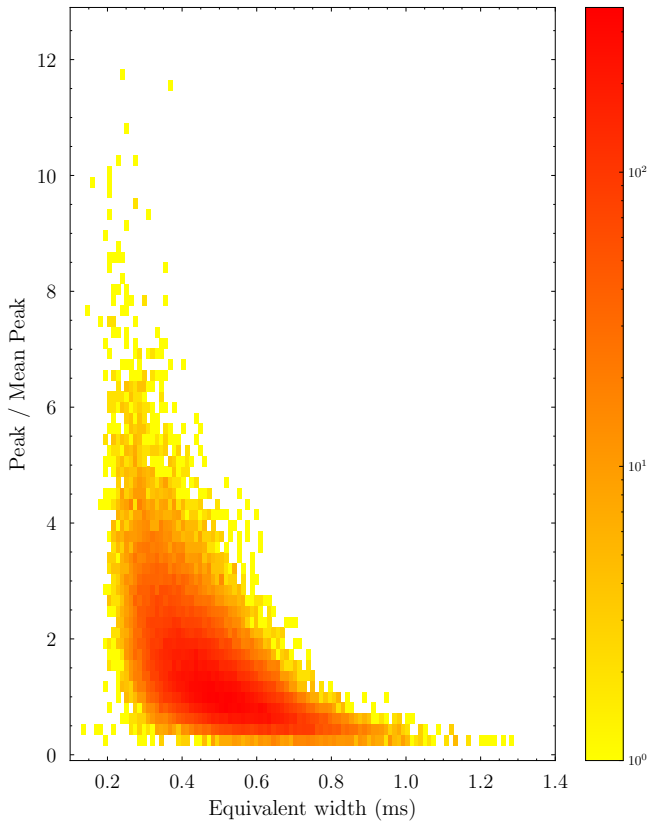


**Figure 6.** The number density distribution of pulses with respect to their relative peak flux densities and the equivalent width  $W_{eq}$ .

of  $m_i$  near the leading peak edge indicates the existence of a tail of bright pulses, which is consistent with the conclusion of Fig. 4. The modulation index  $m_i$  has an asymmetric distribution, meaning that the leading and trailing edges of the integrated profile have a different intensity variation, which is similar to PSR J1713+0747 (Liu et al. 2016).

We use PSRSALSA to obtain the power spectra of the pulse intensity as a function of pulse number and rotational phase, which can reflect the periodicities in the radio emission. This is known as the Longitude Resolved Fluctuation Spectrum (LRFS), which can identify the fluctuation spectrum of constant pulse longitude in the pulse stacks (Backer 1970). The LRFS uses a Discrete Fourier Transform (DFT) to reveal the presence of periodicities for each pulse longitude bin. The middle panel in Fig. 7 shows the LRFS result, where the horizontal axis is  $P/P_3$ , and  $P$  is the pulsar spin period, and  $P_3$  is the sub-pulse pattern repetition rate, namely the period of sub-pulse drifting. There are two maxima values, one at 0.28 cycles-per-period (cpp) and one near 0 cpp. The LRFS is a one-dimensional DFT, and it can not distinguish whether periodic changes of a constant phase bin are due to intensity modulation or sub-pulse drifting.

To distinguish between these possibilities, we must introduce the Two-Dimensional Fluctuation Spectrum (2DFS), obtained by performing DFTs along lines with different slopes in the pulse stack (Edwards & Stappers 2002). The 2DFS does not only give information about the periodic intensity variation along the pulse stack but also provides information on the horizontal separation of the drifting in pulse longitude, namely  $P_2$ . We calculate the 2DFS and plot it in the bottom figure of Fig. 7. We note an offset from the vertical axis

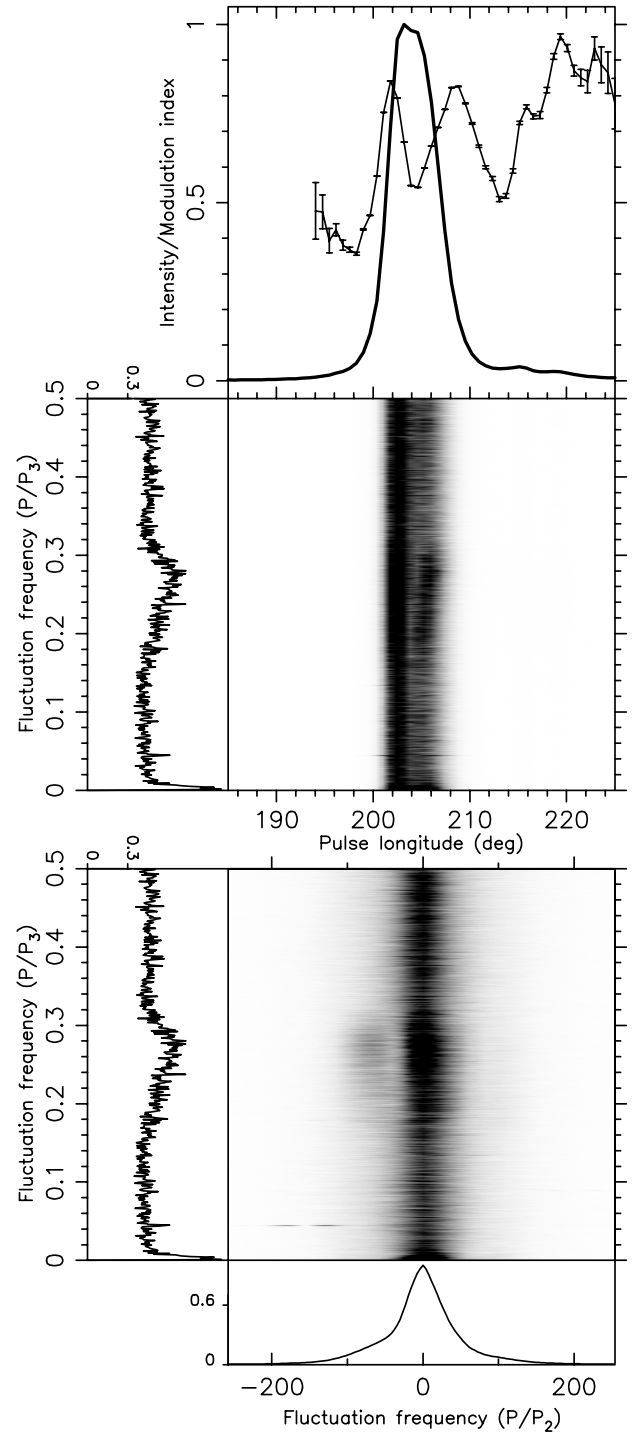


**Figure 7.** The top panel shows how the modulation index  $m_i$  varies with the spin phase, the solid line is the integrated profile, and the points with error bars are  $m_i$ . The middle panel is the LRFS. 2DFS is below the LRFS, and the power in the 2DFS is vertically integrated and normalized with respect to the peak to obtain the bottom panel. Both the LRFS and the 2DFS are horizontally integrated and normalized with respect to the peak to obtain the left panels of the spectra.

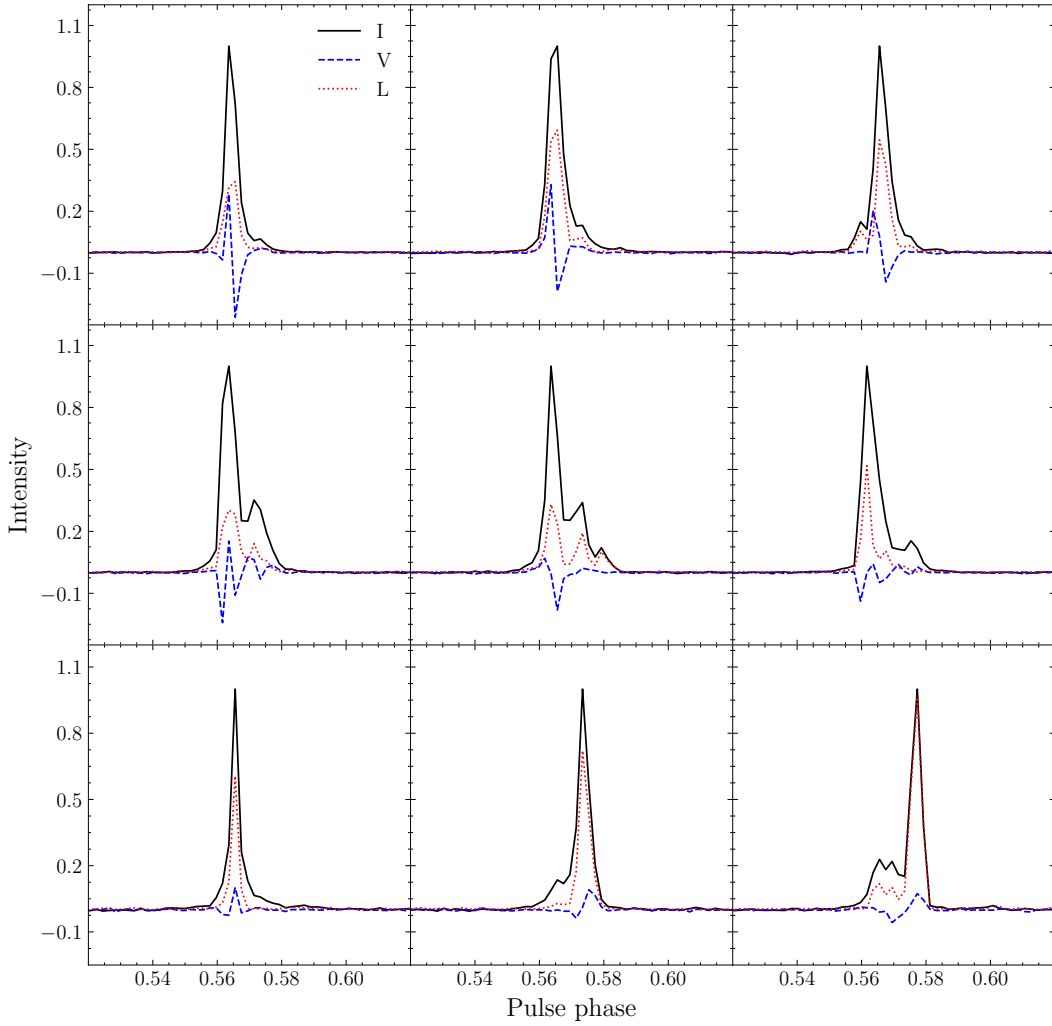


**Figure 8.** The nine high SNR single-pulse polarization profiles. The black solid line is the total intensity  $I$ , the red dotted line is linear polarization intensity  $L$  and the blue dashed line is circular polarization  $V$ . The time resolution in this figure is  $64.06 \mu\text{s}$ .

of zero at  $0.28 \text{ cpp}$  (corresponding  $P_3 \approx 3.5 P$ ) in the bottom panel of Fig. 7, corresponding to a possible systematic drifting of emission power in the pulse phase. The horizontal separation of the drifting in pulse longitude  $P_2 \sim -5.8^\circ$ . The values of  $P_2$  and  $P_3$  are not evident. So there is a weak systematic drifting of emission power in the pulse phase.

### 3.2 Single pulse polarization

The MJD 59209 observation can help us to investigate the polarization properties of single pulses from MSPs. We use the Stokes parameters  $I$ ,  $Q$ ,  $U$ , and  $V$  to describe the polarization of single pulses.  $I$  is the total intensity,  $V$  is the intensity of circular polarization, and  $L = \sqrt{Q^2 + U^2}$  define the linear polarization. We plot nine single-pulse polarization profiles in Fig. 8. The high SNR of these single pulses provides transparent information on circular and linear polarization. In Fig. 8, the top and middle panels show single pulses with a rapid sign change of circular polarization. We note that for some single pulses of PSR J2222–0137, the timescale for the change in circular polarization from a negative to a positive peak is about  $0.15 \text{ ms}$ . Such rapid sign change of circular polarization may originate from an intrinsic mechanism, e.g., the LOS sweep

across the central trajectory of charged bunches (Wang et al. 2022). It could also be caused by propagation effects (Sazonov 1969; Melrose 1997). In Fig. 8, the bottom panel shows single pulses with high linear polarization.

As mentioned above, Guo et al. (2021) have first analysed the integrated polarization profile of PSR J2222–0137 with the data used in this paper. In Fig. 3 of that work, the bottom panel shows values of the PPA of the linear emission as a function of the longitude. The authors used a RVM to fit the black PPA values, and the gray PPA points, which correspond to the rapid changes in PPA, are not fitted. The rapid change region of PPA corresponds to the sudden drops in linear polarization intensity and the very rapid variation in circular polarization intensity, and the authors suggested that this may imply the existence of OPMs.

To reveal if there are OPMs in the grey region, we use the same data to calculate the PPA distribution of single pulses of PSR J2222–0137. Fig. 9 shows the resulting PPA distribution with the spin phase corresponding to the grey region in Fig. 3 of Guo et al. (2021). The red dots are the PPA values of the integrated profile. We note that the PPA distribution of single pulses shows the same trend as the PPA of the integrated profile. There is no evidence for discontinuities of approximately  $90^\circ$  of the single pulse PPA values between spin

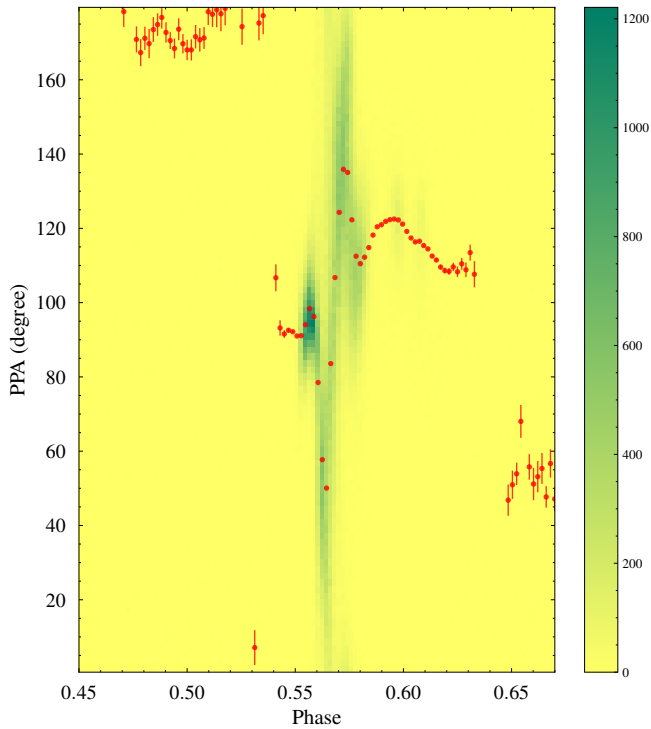


**Figure 9.** The longitude-resolved probability density distribution of PPA values from single pulses of PSR J2222–0137. The values are selected if the corresponding linear polarization SNR > 15 and the error of PPA is less than  $10^\circ$ . The red dots with the error bar are the PPA values from the integrated profile. We only plot the spin phase between 0.52–0.62, corresponding to the region of rapid changes in PPA and V for the integrated polarization profile.

phase 0.52–0.62 at  $64.06 \mu\text{s}$  time resolution. From these data, it is not obvious that OPMs for PSR J2222–0137 exist in this spin phase region. However, a steep transition between modes could still exist at higher time resolutions.

### 3.3 Single pulse jitter

For a same integration time scale, MSPs have more stable integrated pulse profiles than normal pulsars, enabling precision TOAs. This greater stability may be simply due to the much larger number of pulses added for a same time (see chapter 8 in [Lorimer & Kramer 2005](#)). For MSPs’ single pulses, the shape and arrival phase of pulse to pulse could change dramatically, called the “pulse jitter”. The existence of jitters can cause TOA fluctuations even when derived from integrated profiles, contributing to an additional TOA measurement error. We can express the relation as ([Liu & et al. 2011](#)),

$$\sigma_{\text{obs}}^2 = \sigma_{\text{rn}}^2 + \sigma_{\text{J}}^2 + \sigma_{\text{sc}}^2, \quad (5)$$

where  $\sigma_{\text{obs}}$  is the actual measurement uncertainty of the TOA,  $\sigma_{\text{rn}}$  is the uncertainty induced by radiometer noise,  $\sigma_{\text{J}}$  is the uncertainty induced by pulse jitter and  $\sigma_{\text{sc}}$  is induced by instability of short-term diffractive scintillation. For PSR J2222–0137, the contribution of  $\sigma_{\text{sc}}$  can be ignored<sup>5</sup>. The Eqs. (4) and (5) in [Liu & et al. \(2011\)](#) provide

<sup>5</sup> The scintillation frequency is  $\Delta\nu = 30.7 \pm 6.5$  MHz and the scintillation time scale is  $\Delta t = 11.1 \pm 2.3$  min. We use the Eq.(4) in [Shannon & Cordes \(2012\)](#), and for 30-s integration time, we get the rms time error contributed by diffractive scintillation,  $\Delta t_{\text{DISS}} \sim 3$  ns.

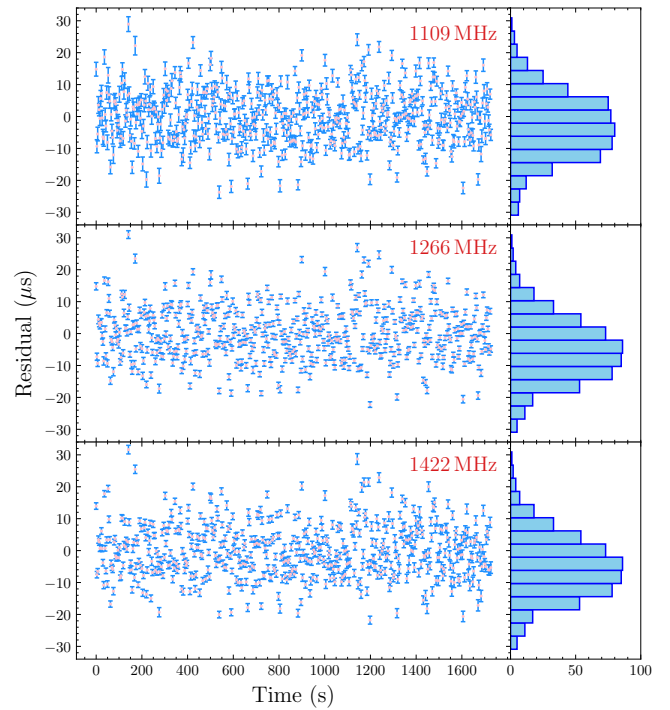


**Figure 10.** The left panels are residual TOAs for observations obtained simultaneously in three sub-bands of 31.25 MHz. The centre frequencies of the bands are 1109 MHz for the top panel, 1266 MHz for the middle panel, and 1422 MHz for the bottom panel. The right panels are histograms of the time residuals of the TOAs.

the formalism of  $\sigma_{\text{rn}}$  and  $\sigma_{\text{J}}$ , and they are all proportional to  $1/\sqrt{N}$ , namely,  $\sigma_{\text{obs}}^2(N) = \sigma_{\text{rn}}^2(N) + \sigma_{\text{J}}^2(N)$ , where  $N$  is the integrated number of pulses.

[Shannon & Cordes \(2012\)](#) plotted the correlation of TOA timing residuals between different frequency sub-bands, showing high correlations. They suggested that such high correlations between different bands could not originate from radiometer noise and demonstrated that they should result from pulse-to-pulse jitter. They calculated CCFs for the TOA residuals between the different sub-bands, and the value at zero lag reflected  $\sigma_{\text{J}}$ , namely  $\text{CCF}(0) = \sigma_{\text{J}}^2$ . Similar to their work, we perform a correlation analysis for residuals at different frequencies. We divide the 500-MHz bandwidth into 16 sub-bands of width  $\Delta f = 31.25$  MHz. We integrate 100 single pulses to form one TOA and use TEMPO to get timing residuals of 16 frequency bands. Fig. 10 illustrates the residuals in three different frequency bands. The errors of TOAs are much smaller than the residual scatter, so the radiometer noise makes a small contribution to  $\sigma_{\text{obs}}$ . Fig. 11 shows the correlation of the residuals between two frequency channels ( $f_x = 1109$  MHz,  $f_y = 1422$  MHz). We can observe a strong correlation between the residuals of the two frequency sub-bands. This indicates that the timing RMS of PSR J2222–0137 is primarily influenced by jitter noise.

We calculate the CCF(0) between different frequency bands with 500 single-pulse integration (integration time = 16.4 s), and the results are shown in Fig. 12.  $\text{CCF}(0) = 12.47 \mu\text{s}^2$ , namely  $\sigma_{\text{J}}(500) \approx 3.53 \mu\text{s}$ , corresponding to jitter of single pulses of  $\sqrt{500} \times 3.53 \mu\text{s} \approx 78.93 \mu\text{s}$ . We use this method to calculate  $\sigma_{\text{J}}$  for different numbers  $N$  of averaged pulses, and the results are shown in Fig. 13. It confirms that jitter noise is the main contributor to  $\sigma_{\text{obs}}$ .

On the other hand,  $\sigma_{\text{obs}}(N)$  is related to  $\sigma_{\text{rn}}(N)$  and  $\sigma_{\text{J}}(N)$ , so we

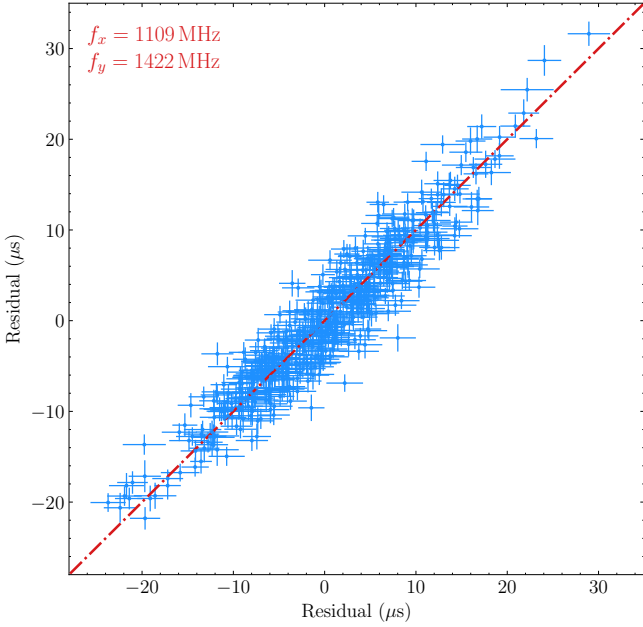


**Figure 11.** The correlation of the TOA residuals between the frequencies 1109 MHz and 1422 MHz. The error bars represent the  $1\text{-}\sigma$  template fitting errors. The red dashed line corresponds to the point where the residuals for the two frequency bands are equal.

can calculate  $\sigma_J(N)$  by,

$$\sigma_J(N) = \sqrt{\sigma_{\text{obs}}^2(N) - \sigma_{\text{rn}}^2(N)}. \quad (6)$$

We calculate  $\sigma_{\text{rn}}^2(N)$  for different pulse numbers  $N$ , and use Eq. (6) to get  $\sigma_J(N)$ . We plot results in Fig. 14, and note that the variation in  $\sigma_J$  with  $N$  is consistent with Fig. 13. Hence, two methods produce consistent results for  $\sigma_J(N)$ . Theoretically,  $\sigma_J(N)$  is proportional to  $1/\sqrt{N}$ . We use  $\sigma_J(N) = \alpha N^\beta$  to fit the variation with  $N$  in Fig. 14, and get  $\alpha = 68.52 \pm 1.48 \mu\text{s}$  and  $\beta = -0.48 \pm 0.01$ , confirming that it satisfies  $\sigma_J \propto 1/\sqrt{N}$ . With values of  $\alpha$  and  $\beta$ , for such high SNR, we can predict jitter noise at 1 hr,  $\sigma_J(1 \text{ hr}) = 270 \pm 9 \text{ ns}$ . So, for high SNR data of PSR J2222–0137 from FAST, the TOAs’ noise is dominated by jitter noise.

Despite this, FAST timing is still more precise than the observations taken by other telescopes. For 15-min integrations, we can get  $\sigma_J(15 \text{ min}) = 519 \pm 20 \text{ ns}$ , the radiometer noise  $\sigma_{\text{rn}}(15 \text{ min})$  is  $\sim 140 \text{ ns}$  (mean value). Thus, for 15-minute observations, the TOA precision is jitter-dominated. Nevertheless, it is still substantially better than what has been achieved to date: Table 2 of Guo et al. (2021) provides the weighted residual RMS  $\sigma_{\text{obs}} = 2.27 \mu\text{s}$  for 900 s TOAs from the Effelsberg telescope at a 1.4 GHz frequency band. Hence, despite the fact that FAST observations of PSR J2222–0137 are affected by jitter noise, they will still represent a significant improvement in the timing precision for this pulsar.

#### 4 CONCLUSION AND DISCUSSION

In our work, we report the study of 52692 single pulses from a high-SNR 30-minute observation of the recycled pulsar PSR J2222–0137 and analyse their statistical properties. The energy distribution of the main-pulse region shows a log-normal distribution, which means that this system has no detectable nulling, mode changes, or giant pulses.

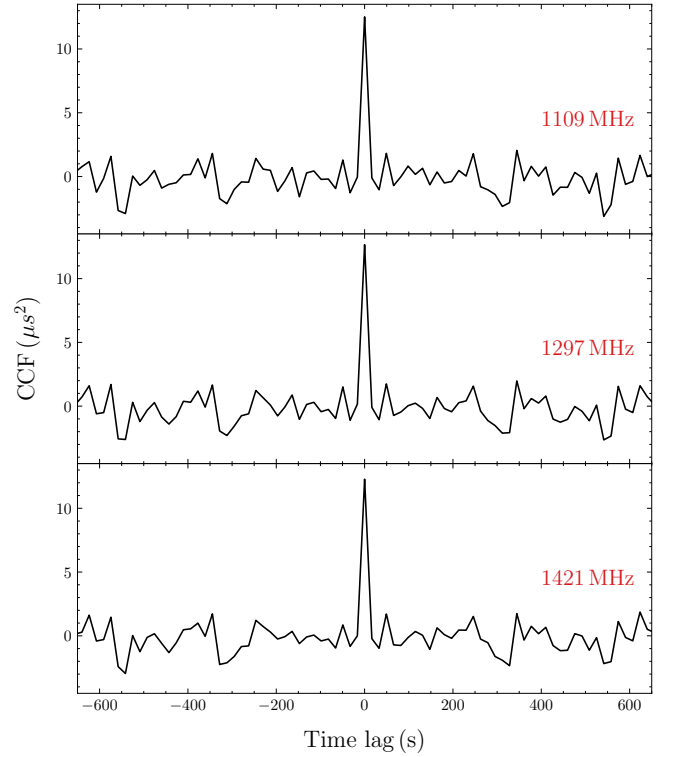


**Figure 12.** The cross-correlation function of 500 single-pulse integrations between time series for the center frequency 1266 MHz and three other frequency bands.

We get the LRFS and 2DFS, and the results suggest a weak sub-pulse drifting in the main pulse of PSR J2222–0137, with  $P_2 \sim -5.8^\circ$  and  $P_3 \sim 3.5 P$ . We analyse the polarization of single pulses of the main-pulse region of PSR J2222–0137 and find no evidence for OPMs in the spin phase 0.52 – 0.62 within  $64 \mu\text{s}$  time resolution. There could be a more complicated emission or propagation process leading to the sudden drops in linear polarization intensity and the very rapid variation of circular polarization intensity in the 0.52 – 0.62 spin phase, or the existence of OPMs visible at higher resolution.

We calculate the jitter noise of PSR J2222–0137 with different numbers of integrated pulses. The cross-correlation between different frequency bands and using Eq. (6) both provide a similar variation relation with  $N$ , and the relation is consistent with  $\sigma_J \propto 1/\sqrt{N}$ . The FAST timing data from PSR J2222–0137 is clearly jitter-dominated; in other words, jitter noise is now the main factor limiting the timing precision, especially for the observations where scintillation significantly brightens the pulsar. When this happens, increases in the sensitivity of the radio telescope can not improve the timing precision. We need to use longer integration times to enhance the timing precision. At 1.25 GHz, we estimate that the jitter noise contribution is  $\approx 270 \text{ ns}$  for 1-h integration. Despite the fact that jitter disproportionately affects the FAST data on PSR J2222–0137, especially for the brightest observations, the FAST data still significantly improve the overall timing precision.

Batrakov et al. (2023) use the TOA uncertainties of PSR J2222–0137 from FAST to simulate a 10-yr timing campaign of PSR J2222–0137. They use a 15-min integration time to reduce the jitter effect because it is jitter-dominated. They predict that the FAST timing of PSR J2222–0137 will result in much-improved measurements of the masses and geometric parameters and vastly improve the

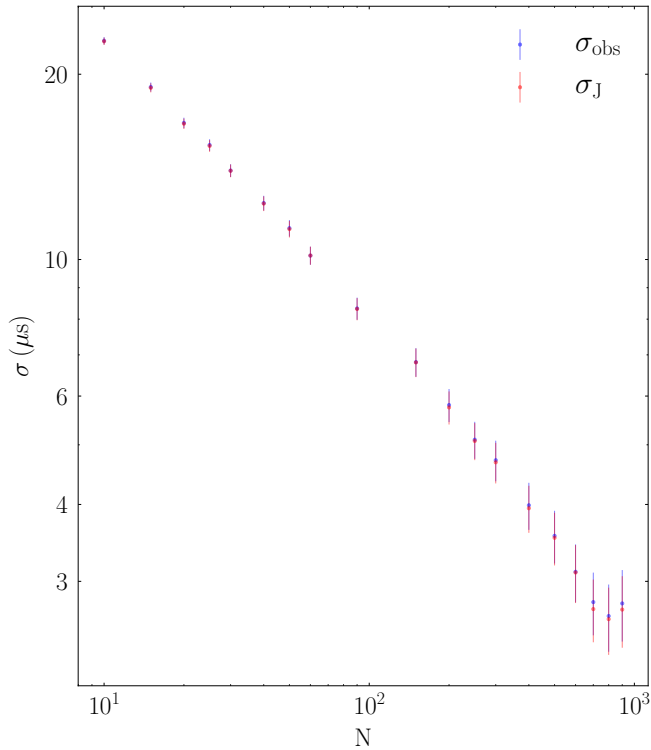


**Figure 13.** The  $\sigma_J$  (red dots) calculated by CCF(0) from different frequency bands ( $\Delta f = 31.25$  MHz). We take an average from the values of CCF(0) of different frequency bands for every fixed number of pulses averaged  $N$ .  $\sigma_{\text{obs}}$  (blue dots) variation with respect to the number of pulses averaged  $N$ .

constraints on the scalar-tensor theories obtained with this system. So, by reasonably arranging timing campaigns of PSR J2222–0137 with FAST, which takes the information on the timing precision into account, these timing data can play an important role in improving the ability to test gravity theories with this system.

#### ACKNOWLEDGEMENTS

We thank the anonymous referee for constructive comments that improved the work. We thank Kuo Liu, Jinchun Jiang, Heng Xu, Dejiang Zhou, Weiyang Wang, Feifei Kou, Yi Feng and Shi Dai for valuable discussions and suggestions. Xueli Miao is supported by the Cultivation Project for FAST Scientific Payoff and Research Achievement of CAMS-CAS. This work was supported by the National SKA Program of China (2020SKA0120200, 2020SKA0120300), the National Natural Science Foundation of China (12203072, 12041303, 12203070), and the CAS-MPG LEGACY project. Jumei Yao is supported by the Natural Science Foundation of Xinjiang Uygur Autonomous Region (grant No. 2022D01D85) and the Major Science and Technology Program of Xinjiang Uygur Autonomous Region (grant No. 2022A03013-2).

#### DATA AVAILABILITY

Origin raw data are published by the FAST data center and can be accessed through them. For other intermediate-process data, please contact the author (xlmiao@bao.ac.cn).

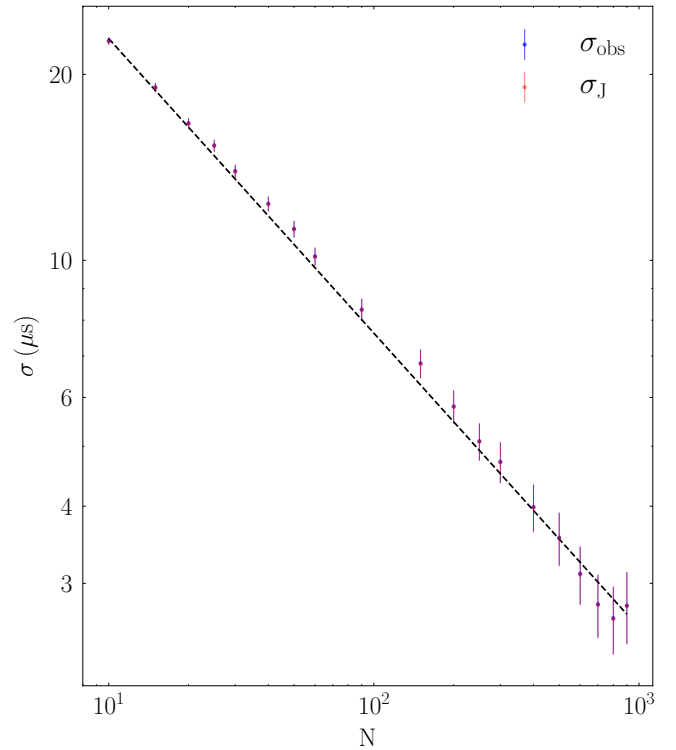


**Figure 14.** The  $\sigma_J$  (red dots) calculated by Eq. (6) and  $\sigma_{\text{obs}}$  (blue dots) variation with respect to the number of pulses averaged  $N$ . The variation of  $\sigma_J$  is same with  $\sigma_J$  calculated by CCF(0) of different frequency bands. The black dashed line is a fit to  $\sigma_J$  with  $\sigma_J(N) = \alpha N^\beta$ , and we get  $\alpha = 68.52 \pm 1.48 \mu\text{s}$  and  $\beta = -0.48 \pm 0.01$  which are similar with the expected scaling  $\sigma_J \propto 1/\sqrt{N}$ .

#### REFERENCES

- Agazie G., et al., 2023, *arXiv e-prints*, p. arXiv:2306.16221  
 Antoniadis J., et al., 2023, *arXiv e-prints*, p. arXiv:2306.16214  
 Backer D. C., 1970, *Nature*, **228**, 42  
 Bartel N., Morris D., Sieber W., Hankins T. H., 1982, *ApJ*, **258**, 776  
 Batrakov A., et al., 2023, A new pulsar timing model for scalar-tensor gravity with applications to PSR J2222-0137 and pulsar-black hole binaries ([arXiv:2303.03824](https://arxiv.org/abs/2303.03824))  
 Cairns I. H., 2004, *ApJ*, **610**, 948  
 Cairns I. H., Johnston S., Das P., 2001, *ApJ*, **563**, L65  
 Cordes J. M., 1993, in Phillips J. A., Thorsett S. E., Kulkarni S. R., eds, *Astronomical Society of the Pacific Conference Series Vol. 36, Planets Around Pulsars*. pp 43–60  
 Cordes J. M., Downs G. S., 1985, *ApJS*, **59**, 343  
 Cordes J. M., Shannon R. M., 2010, *arXiv e-prints*, p. arXiv:1010.3785  
 Cordes J. M., Weisberg J. M., Hankins T. H., 1990, *AJ*, **100**, 1882  
 Damour T., Esposito-Farese G., 1993, *Phys. Rev. Lett.*, **70**, 2220  
 Damour T., Taylor J. H., 1992, *Phys. Rev. D*, **45**, 1840  
 De K., Gupta Y., Sharma P., 2016, *ApJ*, **833**, L10  
 Deller A. T., et al. 2013, *ApJ*, **770**, 145  
 Detweiler S. L., 1979, *Astrophys. J.*, **234**, 1100  
 Drake F. D., Craft H. D., 1968, *Nature*, **220**, 231  
 Eardley D. M., 1975, *ApJ*, **196**, L59  
 Edwards R. T., Stappers B. W., 2002, *A&A*, **393**, 733  
 Edwards R. T., Stappers B. W., 2003, *A&A*, **407**, 273  
 Edwards R. T., Stappers B. W., 2004, *A&A*, **421**, 681  
 Estabrook F. B., Wahlquist H. D., 1975, *General Relativity and Gravitation*, **6**, 439  
 Freire P. C. C., et al., 2012, *MNRAS*, **423**, 3328

- Gil J. A., Lyne A. G., 1995, *MNRAS*, **276**, L55
- Guo Y. J., et al., 2021, *A&A*, **654**, A16
- Hankins T. H., Kern J. S., Weatherall J. C., Eilek J. A., 2003, *Nature*, **422**, 141
- Hellings R. W., Downs G. S., 1983, *ApJ*, **265**, L39
- Hotan A. W., van Straten W., Manchester R. N., 2004, *Publ. Astron. Soc. Australia*, **21**, 302
- Hu Z., Miao X., Shao L., 2023, *arXiv e-prints*, p. arXiv:2303.17185
- Imgrund M., Champion D. J., Kramer M., Lesch H., 2015, *MNRAS*, **449**, 4162
- Jiang P., et al., 2020, *Res. Astron. Astrophys.*, **20**, 064
- Kaplan D. L., et al., 2014, *ApJ*, **789**, 119
- Kramer M., et al., 2021, *Physical Review X*, **11**, 041050
- Liu K., et al. 2011, *MNRAS*, **420**, 361
- Liu K., Eatough R. P., Wex N., Kramer M., 2014, *MNRAS*, **445**, 3115
- Liu K., et al., 2016, *MNRAS*, **463**, 3239
- Liu K., et al., 2022, *MNRAS*, **513**, 4037
- Lorimer D. R., Kramer M., 2005, *Handbook of Pulsar Astronomy*. Cambridge University Press, Cambridge, England
- Melrose D. B., 1997, *Phys. Rev. E*, **56**, 3527
- Mitra D., Arjunwadkar M., Rankin J. M., 2015, *ApJ*, **806**, 236
- Osłowski S., van Straten W., Hobbs G. B., Bailes M., Demorest P., 2011, *MNRAS*, **418**, 1258
- Özel F., Freire P., 2016, *ARA&A*, **54**, 401
- Radhakrishnan V., Cooke D. J., Komisaroff M. M., Morris D., 1969, *Nature*, **221**, 443
- Reardon D. J., et al., 2023, *ApJ*, **951**, L6
- Robinson P. A., 1992, *Sol. Phys.*, **139**, 147
- Sazonov V. N., 1969, *Soviet Ast.*, **13**, 396
- Shannon R. M., Cordes J. M., 2012, *ApJ*, **761**, 64
- Shannon R. M., et al., 2016, *ApJ*, **828**, L1
- Shao L., 2023, in *Proceedings of the Ninth Meeting on CPT and Lorentz Symmetry*. pp 89–93 (arXiv:2208.00142), doi:10.1142/9789811275388\_0019
- Shapiro I. I., 1964, *Phys. Rev. Lett.*, **13**, 789
- Singha J., et al., 2021, *MNRAS*, **507**, L57
- Staelin D. H., Reifenstein Edward C. I., 1968, *Science*, **162**, 1481
- Tauris T. M., van den Heuvel E. P. J., 2023, *Physics of Binary Star Evolution. From Stars to X-ray Binaries and Gravitational Wave Sources*
- Taylor J. H., Weisberg J. M., 1982, *ApJ*, **253**, 908
- Taylor J. H., Weisberg J. M., 1989, *ApJ*, **345**, 434
- Voisin G., Cognard I., Freire P. C. C., Wex N., Guillemot L., Desvignes G., Kramer M., Theureau G., 2020, *A&A*, **638**, A24
- Wang N., Manchester R. N., Johnston S., 2007, *MNRAS*, **377**, 1383
- Wang W.-Y., Yang Y.-P., Niu C.-H., Xu R., Zhang B., 2022, *ApJ*, **927**, 105
- Weltevrede P., 2016, *A&A*, **590**, A109
- Weltevrede P., Edwards R. T., Stappers B. W., 2006, *A&A*, **445**, 243
- Wex N., 2014, in *Kopeikin S. M., ed., , Vol. 2, Frontiers in Relativistic Celestial Mechanics: Applications and Experiments*. Walter de Gruyter GmbH, Berlin/Boston, p. 39 (arXiv:1402.5594)
- Xu H., et al., 2021, *The Astronomer’s Telegram*, **14642**, 1
- Xu H., et al., 2023, *Research in Astronomy and Astrophysics*, **23**, 075024
- Zhao J., Freire P. C. C., Kramer M., Shao L., Wex N., 2022, *CQGra*, **39**, 11LT01
- van Haasteren R., Levin Y., McDonald P., Lu T., 2009, *MNRAS*, **395**, 1005
- van Straten W., Bailes M., 2011, *Publ. Astron. Soc. Australia*, **28**, 1

This paper has been typeset from a  $\text{\TeX}/\text{\LaTeX}$  file prepared by the author.